Ocean Sci. Discuss., 12, 3003–3041, 2015
www.ocean-sci-discuss.net/12/3003/2015/
doi:10.5194/osd-12-3003-2015

Ocean Science Discussions
Open Access
EGU

Seasonal variability of the Ekman transport and pumping in the upwelling system off central-northern Chile (~ 30° S) based on a high-resolution atmospheric regional model (WRF)

L. Bravo[1,2,3], **M. Ramos**[2,3,1], **O. Astudillo**[1,4], **B. Dewitte**[4,3], **and K. Goubanova**[5,4]

[1]Centro de Estudios Avanzado en Zonas Áridas (CEAZA), Coquimbo, Chile
[2]Departamento de Biología, Facultad de Ciencias del Mar, Universidad Católica del Norte, Coquimbo, Chile
[3]Millennium Nucleus for Ecology and Sustainable Management of Oceanic Islands (ESMOI), Coquimbo, Chile
[4]Laboratoire d'Etudes en Géophysique et Océanographie Spatiales (LEGOS), Toulouse, France
[5]Centre Européen de Recherche et de Formation Avancée en Calcul Scientifique (CERFACS), Toulouse, France

Received: 1 October 2015 – Accepted: 13 November 2015 – Published: 8 December 2015
Correspondence to: L. Bravo (luis.bravo@ucn.cl), M. Ramos (marcel.ramos@ucn.cl)
Published by Copernicus Publications on behalf of the European Geosciences Union.

OSD
12, 3003–3041, 2015

Abstract

Two physical mechanisms can contribute to coastal upwelling, offshore Ekman transport and Ekman pumping due to the cyclonic wind stress curl, mainly caused by the abrupt decrease in wind stress (drop-off) in a cross-shore band of 100 km. This wind drop-off is thought to be an ubiquitous feature in coastal upwelling systems and to regulate the relative contribution of both mechanisms. It has been poorly studied along the central-northern Chile region because of the lack in wind measurements along the shoreline and of the relatively low-resolution of the available atmospheric Reanalysis. Here, the seasonal variability in Ekman transport, Ekman pumping and their relative contribution to total upwelling along the central-northern Chile region ($\sim 30^{\circ}$ S) is evaluated from a high-resolution atmospheric model simulation. As a first step, the simulation is validated from satellite observations, which indicates a proper representation of the spatial and temporal variability of the wind along the coast by the model. The model outputs are then used to document the fine scale structures in the wind stress and wind curl in relation with the topographic features along the coast (headlands and embayments). Both wind stress and wind curl had a clear seasonal variability with a marked semiannual component. Alongshore wind stress maximum peak occurred in spring, second increase was in fall and minimum in winter. When a threshold of -3×10^{-5} s^{-1} for the across-shore wind curl was considered to define the region from which the winds decrease on-shoreward, the wind drop-off length scale varied between 8 and 45 km. The relative contribution of Ekman transport and Ekman pumping to the vertical transport along the coast, considering the estimated wind drop-off length, indicated meridional alternation between both mechanisms, modulated by orography and the intricate coastline. Roughly, coastal divergence predominated in areas with low orography and headlands. Ekman pumping was higher in regions with high orography and the presence of embayments along the coast. In the study region, the vertical transport induced by coastal divergence and Ekman pumping represented 60 and 40 % of

OSD
12, 3003–3041, 2015

the total upwelling transport, respectively. The potential role of Ekman pumping on the spatial structure of sea surface temperature is also discussed.

1 Introduction

In the eastern boundary current systems wind-induced upwelling has mainly been described using two primary mechanisms (Sverdrup et al., 1942; Gill, 1982; Pickett and Paduan, 2003; Capet et al., 2004; Jacox and Edwards, 2012). The first one is coastal divergence which is the result of offshore Ekman transport due to alongshore winds (with an equatorward component) and earth's rotation. The second one is Ekman pumping which is the result of a cyclonic wind stress curl caused mainly by the wind drop-off that ribbons only tens of km in width along the coast, a typical feature of the eastern boundary current systems (Bakun and Nelson, 1991; Pickett and Paduan, 2003; Capet et al., 2004; Jacox and Edwards, 2012). Starting in the mid 1970s, a series of studies began assessing the contribution of Ekman pumping on coastal upwelling for the California Current System (Halpern, 1976; Nelson, 1977), which later expanded to the other four upwelling systems (Bakun and Nelson, 1991). In one of these four regions, the coast of north and central Chile, this mechanism has been poorly evaluated, primarily due to limitations in diffusiometer winds that have a "blind zone" near the coast and the relatively low spatial resolution of the atmospheric Reanalyses. This has limited progresses in the understanding of the upwelling dynamics and the coastal circulation of the region, among other factors.

Coastal upwelling has been widely studied in several regions of the world, in particular along the Eastern Boundary Upwelling Systems (EBUS). Currently, there is no generalized conceptual model for the upwelling structure that considers the region near the coast, the coastal boundary and the open ocean (Mellor, 1986; Marchesiello and Estrade, 2010). Traditionally a simple relationship based on wind stress along the coast has been used as an index of the coastal upwelling intensity (Bakun, 1973), this approximation does not consider other more complex physical processes, such as the wind

OSD
12, 3003–3041, 2015

curl (Pickett and Paduan, 2003; Capet et al., 2004; Jacox and Edwards, 2012) and the geostrophic flow toward the coast, which is in balance with the along shore pressure gradient and could potentially limit upwelling (Marchesiello et al., 2010; Marchesiello and Estrade, 2010). In the case of the wind curl, several modeling studies from different upwelling systems, suggest that wind stress decreases within a narrow coastal band of 10–80 km called wind "drop-off" (Capet et al., 2004; Bane et al., 2005; Perlin et al., 2007; Renault et al., 2012, 2015) that is very sensitive to the resolution of the model. Thus, regional ocean modeling studies show that the upwelling response is very sensitive to the transition in the structure of the wind near the coast (Capet et al., 2004; Jacox and Edwards, 2012), where the structure and physical forcing of the transitional coastal wind profile is not well understood (Jin et al., 2009). In the literature at least three main hypotheses have been proposed to explain the decrease of onshore wind (drop-off) that generates the wind stress curl within the coastal band. The first is related to the change of surface and boundary layer friction in the land–sea interface (Capet et al., 2004). The second is related to the ocean–atmosphere coupling between the sea surface temperature (SST) and the wind (Chelton et al., 2007), particularly cold water upwelling tend to stabilize the atmospheric boundary layer, decoupling the high atmospheric circulation with the surface circulation. The last one is related to coastal orography (Edwards et al., 2001), coastline shape (Perlin et al., 2011), and the combination of both (Renault el at., 2015). Other possible mechanisms that could potentially contribute to wind drop-off near the coast are the effects of sea breeze and pressure gradients (across or along the coast) at sea level.

The central-northern Chile region is characterized by nutrient rich cold surface waters, attributed to the surface circulation of the Humboldt system and mainly coastal upwelling driven by along shore winds that are associated with the southeast Pacific anticyclone (Shaffer et al., 1999; Halpern, 2002). A strong seasonal variability of the southeast Pacific anticyclone produces favorable upwelling winds to peak during spring and summer and decrease during winter (Strub et al., 1998). Within central-northern Chile the area around 30° S is characterized by the most intense upwelling favorable

OSD
12, 3003–3041, 2015

winds (Shaffer et al., 1999; Rutllant and Montecino, 2002). Additionally, local high frequency forcing in the region is associated with atmospheric coastal jets with periods less than 25 days (Garreaud and Muñoz, 2005; Muñoz and Garreaud, 2005) that are related to the variability of the South Pacific anticyclone and play a major role in coastal upwelling (Renault et al., 2009, 2012; Aguirre et al., 2012). All these features make the region a natural laboratory to explore the forcing mechanisms and describe the physical processes that modulate coastal upwelling.

In a recent modeling study Renault et al. (2012) analyzed the main physical processes that explain changes in sea surface temperature in an upwelling event during the passage of an atmospheric coastal jet along the central-northern Chile region. The results showed a clear drop-off of the coastal wind that was not observed in the QuikSCAT data, due to a "blind zone" in the satellite measurements (~ 25 km offshore). The oceanic response to the atmospheric coastal jet produced significant cooling of the sea surface that significantly contributed to ocean vertical mixing equivalent to the magnitude of the vertical advection near the coast. Their sensitivity analyses showed that the response of the coastal ocean highly depends on the representation of the wind drop-off. This is because the total upwelling (i.e. the sum of coastal upwelling and Ekman pumping) depends on the scale of the wind drop-off. The authors suggest there is a negative effect on coastal upwelling, due to a reduced Ekman transport near the coast that is not balanced by Ekman pumping. In addition, the drop-off has a strong effect on vertical mixing and consequently the cooling of the coastal ocean. In a previous modeling study Capet et al. (2004) off the coast of California suggested that a poor representation of the wind drop-off could underestimate Ekman pumping and overestimate coastal upwelling (and vice versa), with consequences for the coastal circulation processes. Meanwhile, Garreaud et al. (2011) using observations found a local atmospheric coastal jet just north of one of the most prominent geographic points of the region: Punta Lengua de Vaca (see Fig. 1). This coastal jet presents a distinct daily cycle as the result of the strong baroclinicity due to heating differential in the region. In a later study Aguirre et al. (2012) using climatological QuikSCAT winds to force an

OSD
12, 3003–3041, 2015

ocean model, found the importance of the wind stress curl over the regional circulation exerting control over the seasonal cycle of an Equatorward coastal jet. This study also evaluated the contribution of Ekman pumping to the total upwelling, which was not resolved due to a poor resolution of the satellite winds within the first 30 km near the coast. In particular, due to the narrow continental shelf off central-northern Chile, the cells of upwelling due to coastal divergence are trapped near the coast (Estrade et al., 2008), consequently the use of QuikSCAT winds could be overestimating the effect of upwelling driven by coastal divergence and Ekman pumping.

Although previous studies have documented the importance of the wind stress curl near the coast of central Chile (Renault et al., 2012; Aguirre et al., 2012), the impact of this abrupt transition of the wind near the coast (i.e. drop-off) and its seasonal variability on upwelling are still poorly understood. Here, prior to addressing this issue from an oceanic perspective, our objective is to document the wind stress curl (drop-off) and its seasonal variability off central-northern Chile ($\sim 30^{\circ}$ S) using a high resolution (~ 4 km) atmospheric model. Our focus in on the Ekman pumping and its contribution to the total upwelling, and the factors that could contribute to its meridional variability (i.e. topography, coastline and air–sea interactions).

The paper is organized as follow: a description of the atmospheric simulations and the methods used to estimate different upwelling terms are described in Sect. 2. The following section presents results and discussions and was subdivided into three subsections. The first one describes wind stress curl pattern and the spatial scale of the wind drop-off. The second one presents an analysis of the annual variability in Ekman Pumping and coastal divergence, their relationship with coastal topography and their contribution to upwelling transport. Finally, the study relates Ekman Pumping transport to sea surface temperature near the coast.

OSD
12, 3003–3041, 2015

2 Methods and model configuration

2.1 Model output

The Weather Research and Forecasting (WRF) model version 3.3.1 (Skamarock and Klemp, 2008) was implemented in a configuration with three nested grids (Fig. 1) increasing the spatial resolution over the region of interest, the use of multiple grid nesting improves the representation of complex terrain and associated processes and has been found to increase the simulation skill of WRF (Horvath, 2012).

The largest synoptic domain covers most of South America and the eastern Pacific in a Mercator projection with a horizontal resolution of 36 km, the second domain corresponds to the Central Chile region with a horizontal resolution of 12 km and the innermost domain is centered over the prominent upwelling region of Coquimbo and has 4 km horizontal grid spacing (Fig. 1). WRF employs a terrain-following hydrostatic-pressure coordinate in the vertical, defined as eta (η) levels, here a total of 42 η levels were used in the vertical with increasing resolution toward the surface, 20 of them in the lowest 1.5 km with $\sim$ 30 m in the vertical for the surface level (Garreaud and Muñoz, 2005).

Initial and lateral boundary conditions for the simulation were derived from the National Centers for Environmental Prediction (NCEP) Final Analysis Data (FNL) (Kalnay et al., 1996; available online at http://rda.ucar.edu/datasets/ds083.2) at $1^{\circ} \times 1^{\circ}$ global grids every six hours, the boundary conditions are prescribed over the coarser domain with the depth of 5 grid-cells where simulated variables are relaxed towards the FNL solution. The SST forcing data are based on the daily Operational Sea Surface Temperature and Sea Ice Analysis (OSTIA) at $0.05^{\circ} \times 0.05^{\circ}$ global grids resolution (Stark et al., 2007).

The model was first evaluated in terms of its sensitivity to the different combinations of parameterizations (cumulus – PBL-soil model) and to the surface boundary forcing (SST forcing, topography and land surface) and nesting modes in order to identify the one that gives the most realistic estimates of observed surface variables. The most

OSD
12, 3003–3041, 2015

realistic configuration in terms of regional surface circulation variability and mean state was then used for simulating the period 2007–2012 at hourly intervals (Table 1).

The atmospheric simulations were validated using QuikSCAT satellite winds and wind observations from two weather stations near the coast in Loma de Hueso (LDH) and Punta Lengua de Vaca (PLV) and a third station farther inland named Parral Viejo (Figs. 1 and 2). A spatial comparison was done using the coarse resolution grid (36 km) between satellite and WRF winds for 2007–2009. The comparison showed a good agreement between observations and modeling results with a similar spatial structure and magnitudes of the same order, especially within the study region (27–33° S). The root mean square (RMS) of the difference for observations and model results was less than 1 m s^{-1} (Fig. 2c). The high-resolution model outputs (4 km) were also compared with available observations. Initially, for each of the weather stations daily wind cycles were compared with simulations (results not shown), the results indicate a better fit in diurnal variability when the model is forced with SST (OSTIA), which was finally chosen for the simulations performed in this study. The best fit between observations and model outputs was found when the wind intensifies during the afternoon between 17 and 19 h, this intensification is described as the result of mesoscale wind forcing in the region (Rahn et al., 2011). A good model representation of the afternoon winds is key for a proper representation of coastal upwelling in the region. Finally, for each weather station, linear regressions and dispersion plots were done between the meridional component of simulated (4 km) and observed winds (Fig. 2d–f), a good agreement was observed for all the cases.

2.2 Upwelling estimates

The relative importance of coastal upwelling due to coastal divergence (Smith, 1968) was estimated using wind stress obtained by the WRF model:

$$M = \frac{1}{\rho_w f}\tau \times \hat{k} \quad (1)$$

OSD
12, 3003–3041, 2015

where M is Ekman transport ($m^3\,s^{-1}\,m^{-1}$ of coast), τ is the wind stress at the land–sea margin (~ 4 km de la costa), ρ_w is water density, f is the Coriolis parameter and k is a unit vector tangent to the local coastline. The vertical velocity from Ekman pumping was estimated using a definition given by Halpern (2002) and Renault et al. (2012).

$$w_{EP} = \frac{\mathrm{Curl}(\tau)}{\rho_w f} + \frac{\beta \tau_x}{\rho_w f^2} \quad (2)$$

where $\tau(x,y)$ is wind stress, β is the Coriolis parameter gradient and τ_x is the cross-shore wind stress. Latitude variations were not significant therefore the last term in Eq. (2) was neglected. In order to compare the two upwelling processes, Ekman pumping was converted into transport by integrating the vertical velocity within a certain distance from the coast, which in our case was the length scale of the wind drop-off (Ld) obtained from a reference value (defined by Renault et al., 2015) where cross-shore wind curl was $< -3 \times 10^{-5}\,s^{-1}$. The wind drop-off spatial length (Ld) varies meridionally (Fig. 3c and d).

Note that if we assume that the wind is parallel to the coast and that the wind curl is dominated by its cross-shore gradient component (and this gradient is nearly constant in the drop-off zone), then the total upwelling transport is simply $\tau/(\rho f)$ or expressed as vertical velocity is $W = \tau/(\rho f\ \mathrm{Ld})$, where τ is the wind stress at Ld. Consequently it is apportioned to Ekman transport and pumping according to the amount of drop-off (for more details see Renault et al., 2012). On the other hand, in our study zone there is a marked decline of onshore wind, therefore the wind drop-off has an impact on the total upwelling velocity. Thus a proper assessment of scales involved in both mechanisms is crucial to the upwelling problem.

OSD
12, 3003–3041, 2015

3 Results and discussion

3.1 Mean wind stress curl and the wind drop-off spatial scale

From the wind stress simulations we obtained the mean of the wind stress curl in the three model domains with spatial resolutions of 36, 12 and 4 km (Fig. 3a–c). The mean wind stress curl patterns show clear differences when resolution is increased. In the simulations of higher resolution small scale or finer structures are well defined, especially close to the coast, that are not present in the simulation of coarse resolution, and that are not resolved or studied in previous studies (Aguirre et al., 2012; Renault el al., 2012). The simulations with higher resolution (12 and 4 km) show a cyclonic wind stress curl (negative) within the coastal band and within the Coquimbo bay system that is associated to a positive Ekman pumping (due to upwelling). While in the oceanic sector a less intense anticyclone wind curl predominates. The negative curl within the coastal band is the result of an onshore decay in wind intensity (drop-off) that is characteristic from EBUS systems (Capet et al., 2004; Renault et al., 2012).

In the central-northern Chile region the drop-off length scale (Ld) is between 8 and 45 km (Fig. 3b and c, segmented yellow line). When the resolution of the model is increased a drop-off scale is more restricted to the shore and with greater spatial structure, with greater extension in the central region of the domain than the region south of 30.25° S. The meridional differences at Ld could be associated to coastal orography and the shape of the coastline; this will be discussed later in Sect. 3.3. The finer structures in the wind stress curl close to shore, cannot be determined from observations of the scatterometers of previous and current satellite missions, such as QuikSCAT and/or other satellite, because of the blind zone in measurements within the first 25 km from the shore, which increases to 50 km when wind stress curl is estimated, as the result of the estimate of the spatial derivative.

Renault et al. (2012) based on atmospheric simulations (obtained with WRF) determined that the extent of the wind drop-off was ∼ 70 km, this length was different from the one obtained in this study (which varied between 8 and 45 km), possibly because of

OSD
12, 3003–3041, 2015

the lower resolution used in their study. To explain the wind zonal structure and drop-off, Fig. 3d shows zonal profiles of the meridional wind of the more exposed region. The results indicate a clear decay of the wind along the coast in the three simulations (36, 12 and 4 km) that is not observed from satellite data from QuikSCAT. It should be noted the small difference with the satellite product. Thus, in the study region there is a scarcity of wind information within the coastal band that covers the blind zone of the satellites and that can be used for validation purpose. One of the first observations in the region was taken during the field campaign CupEX (Garreaud et al., 2011), during this experiment a zonal profile of wind was measured using airborne meteorological techniques. These observations allowed detecting an atmospheric coastal jet with a marked daily cycle that projects north of Punta Lengua de Vaca towards the Coquimbo bay system. This jet is caused by a zonal differential in temperature and the resulting baroclinicity.

Note that this wind structure is displayed in our simulations and produces a wind curl north of the bay, which affects the circulation and coastal upwelling in the region. Recent wind observations were generated under the scope of this study (FONDECYT Postdoctoral project 3130671), and are presented in Fig. 3e. These wind observations were made with a marine weather station (AirMarch) installed on a fishing boat. Measurements were made for 22 April, 18 May, 15 September and 28 October 2014. Although these measurements do not cover the period of the simulations, they are presented here to illustrate observed features of the zonal wind profiles in the southern region. Despite the large spatial and temporal variability of the observations, they suggest a tendency to a reduction of the along-shore winds on-shoreward comparable to what is simulated by the model (Fig. 3d).

3.2 Annual variability of the wind stress and Ekman pumping

The seasonal analysis of the wind stress and the Ekman pumping is based on the simulation having the highest resolution (4 km), considering the daily outputs over the period between 1 January 2007 and 31 December 2012. Figure 4 presents the mean seasonal cycle of the wind stress for the study area in the coastal fringe extending

OSD
12, 3003–3041, 2015

150 km from the coast. The wind stress presents seasonal and spatial variability, with predominance of upwelling favorable winds (with equator-wards component) during all the year round, with maximum values ($\sim 0.15\,\mathrm{N\,m^{-2}}$) between September and November, which is characteristic of the central-northern region of Chile (Shaffer et al., 1997; Rutllant and Montecino, 2002; Ranh and Garreaud, 2013). The seasonal variability of the wind stress determines behavior of coastal upwelling and primary productivity in the region. This is through two main mechanisms, the coastal divergence and the Ekman pumping, that will be evaluated in the following sections. The wind can also induce vertical mixing and in turn surface cooling; this could even be of the same order of magnitude as the vertical advection (Renault et al., 2012). In general, these mechanisms may covary in time, responding to the seasonal cycle of the wind stress; hence in a grouped statistical analysis (like SVD) it is difficult to isolate the spatio-temporal combined variability of two mechanisms without rejecting the effect of the third. On the other hand, the model simulates well the coastal atmospheric jet observed in the zone of Punta Lengua de Vaca ($\sim 30^{\circ}$ S), in particular the maximum intensity during spring (Rahn and Garreaud, 2011, 2013).

Close to the coast, where the satellite data have no coverage or the estimate in wind stress is uncertain (Fig. 1), a wind decay towards the coast (drop-off) is observed during practically all the months of the year, with still a more pronounced tendency in the period between September and December. The horizontal gradient of the wind stress that is most intense close to the coast produces a wind curl with a clockwise rotation direction (cyclonic for the SH) generating a positive Ekman pumping favorable to the upwelling.

In addition to a non-uniform spatial distribution, the drop-off length (Ld) in the area of interest also exhibits a marked seasonal variability. Through an atmospheric simulation in the west coast of USA, Renault et al. (2015) also suggested that the drop-off presents seasonal and spatial variability, but with an extension ranging from between 10 to 80 km. These authors propose that the drop-off dynamics of the wind is due mainly to orographic effects and the shape of the coastline, reaching a maximal reduc-

OSD
12, 3003–3041, 2015

tion of the wind (∼ 80 %) when these are combined. According to these authors, the drop-off length scale of the wind in front of Chile should be approximately 30 km, less than the scale off the west coast of USA. According to the authors, this would result from the different shape of the Chilean coast line characterized by astraighter coastline and the reduced numbers of capes compared to the US West coast. In addition the Andes induce a sharper decline of wind (drop-off) than the mountains of the west coast of the USA. In the Sect. 3.3 the length scale of the drop-off along the central-north coast of Chile will be analyzed in relation with the coastal orography and the shape of the coastline.

Despite that the drop-off extension in front of central-northern Chile (∼ 45 km) is on average weaker than that estimated in the California currents system (Enriquez y Friehe, 1996; Renault et al., 2015), the wind-stress curl from this zonal gradient of the wind generates an Ekman pumping with a marked seasonality (Fig. 5) and positive vertical velocities (to the surface) that reach 4 m day^{-1}, similar values to that obtained by Pickett and Paduan (2003) in front of the region of the California current system.

The simulation (4 km) has allowed to depict and document the mesoscale atmospheric circulation in the first 50 km of the coast (Fig. 3), where the spatial patterns of the Ekman pumping are much more marked, especially at latitudes where there are sharp topographic changes in the coastline (Fig. 5). Thus, structures of Ekman pumping are highlighted to the north of the main headlands of the region (Punta Lengua de Vaca and Punta Choros), and show a seasonal cycle. In addition, the Ekman pumping presents negative values (downwelling) off shore associated to an anti-cyclonic wind curl around 28.5° S and between 30 and 31° S that reaches the greatest extent during August, while decreasing considerably in the summer months and beginning of fall (Fig. 5). The difference for the Ekman pumping between the mean spring and the rest of the seasons (i.e. summer, fall and winter) indicate that the spring positive pumping dominates the other, specially north of 29° S, in the interior of the Coquimbo bay system and south of 31.5° S (Figure not shown).

OSD
12, 3003–3041, 2015

With the objective of analyzing in more details the seasonal and spatial variability of the wind stress and the zonal gradient, three specific sectors of the interest area were selected (28.5, 30.5 and 32.5° S), that are out of the Coquimbo bay system (Fig. 6). As was mentioned before, the region is characterized by a marked wind stress seasonality more pronounced to the south of the interest area (Fig. 6c). In general, the wind component along the coast presents values favorable to the upwelling during all the year round, emphasizing a decrease in the wind stress towards the coast for the spring and summer months at 32.5° S, and in summer at 28.5 and 30.5° S. When estimating the zonal gradient of the wind stress taking as a reference the wind at the coast, the most intense positive gradients (due to the wind drop-off towards the coast) are obtained in a coastal band with a width smaller than 50 km, indicating that the Ekman pumping is the most effective inside the coastal band, as is evidenced in the Figs. 4 and 5. On the other hand, the negative zonal gradient extent (Ekman pumping and downwelling) is greater in the sections located more to the north, at 28.5 and 30.5° S, than in that located at 32.5° S (Figs. 6d–f), indicating that in the southern part of the study region, the positive Ekman pumping region is more extensive than in the zones where the wind stress is more intense seasonally close to the coast (Fig. 4).

3.3 Contributions of Ekman transport and Ekman pumping to the upwelling rate

The central-northern Chile continental shelf is very narrow and very steep so the scale of coastal divergence is < 10 km (considering the theoretical framework of Estrade et al., 2008), while the scale of Ekman pumping considering Ld scale (previously defined, based on Renault et al., 2015) is ~ 45 km. To compare the seasonal contribution of coastal divergence and Ekman pumping to the total transport of coastal upwelling in the study region, the annual cycle of coastal divergence was obtained first by taking the wind measurement closest to the coast and meridionally integrated every 0.25° (Fig. 7c), while the annual cycle of Ekman pumping transport was obtained by integrat-

OSD
12, 3003–3041, 2015

ing the vertical velocity from the shoreline to the distance corresponding to the drop-off (Ld) value, also within 0.25° latitude bands (Fig. 7d).

The results show a marked annual cycle with maximum vertical transport in the spring, both induced by coastal divergence and Ekman pumping, with secondary maximum in some areas during autumn accounting for a weaker semiannual component. As expected, there is a large temporal coherency along the coast between both processes (the meridionally average correlation between Ekman pumping and transport reaches 0.8), except locally at some latitudes (e.g. at 31.25° S) where there is a weak seasonal cycle in Ekman pumping (Fig. 7d) due either to a weak drop-off or a compensation effect by the zonal wind stress component. The high correlations indicate a seasonal consistency between both mechanisms, which has been previously reported in other upwelling systems (e.g. Pickett and Paduan, 2003; Renault et al., 2015). Although both mechanisms are highly correlated at seasonal timescales, they exhibit significant differences in relative magnitude as a function of latitude, i.e. when one is intense the other is weak. For instance, coastal divergence strongly dominates over Ekman pumping between 30.25–31.25° S, which is the most recognized upwelling center in the region (located south of PLV), which is also the case between 28.5–29.25° S (north of Punta Choros). In these sectors Ekman pumping tends to be weaker, while predominant between 29.25–30.25° S, inside the Coquimbo bay system and between 28.0–28.75° S, north of LDH. South of 31.25° S, both mechanisms varies meridionally more uniformly. The estimate of the meridional correlation between both mechanisms as a function of calendar month, indicates that they are more related in spring and summer (~ -0.72) than in winter (~ 0.45). Possible processes that could explain the inverse (negative) spatial relationship between the two mechanisms and its seasonal modulation are discussed below.

Following the recent study by Renault et al. (2015), we now document the relationship between the relative importance of Ekman transport and pumping, and the coastal topography and shape of the coastline in the region. An along-coast orography index (H_{index}) is estimated from the average of the orographic height between the coastline

OSD
12, 3003–3041, 2015

and 100 km inland (as in Renault et al., 2015). In addition, the coastline meandering index (M_{index}) is estimated using a high-pass along-shore filter (with 10 km half-width) applied to the coastal longitude (Renault et al., 2015). Figure 7a shows the H_{index} (black line) and M_{index} (red line). In the latter index negative values are associated with headlands, while positive values are associated with bays. The drop-off scale and alongshore wind at the coast and at Ld are also included (Fig. 7b and c). Note that Ld is inversely proportional to coastal wind (R^2 de ~ 0.81), while the wind evaluated at Ld is spatially more homogenous. This differs from the results obtained by Renault et al. (2015) along the western coast of USA. From the inspection of H_{index}, M_{index} and Ld three scenarios are defined that could explain the observed upwelling pattern (Fig. 7d and e):

1. Prevalence of positive Ekman pumping: in sectors such as the Coquimbo bay system and the region north of 28.5° S (LDH), where the wind curl intensifies due to the sharp decline of onshore wind, with a large drop-off scale (Ld). In addition, the combination of a high orography (large H_{index}) and the presence of bays and headlands along the coastline favor a decrease in the meridional onshore wind.

2. Prevalence of coastal divergence: in sectors characterized by a low topography (small H_{index}) and a negative M_{index} due to the presence of headlands such as Punta Lengua de Vaca and Punta Choros, with a drop-off scale (Ld) smaller and stronger winds alongshore (Fig. 7b and c).

3. South of 31.25° S the pattern is more complex than previous scenarios. Both mechanisms are present but with a slight dominance of coastal divergence on Ekman pumping. South of this latitude, Ld increases, coastal wind decreases and wind curl increases (Fig. 7b and c). M_{index} shows the presence of small inlets and headlands and the orograpahy index is moderate high without largest changes as in the northern coastal region.

Renault et al. (2015) proposed that the coastal topography induces a decrease in the intensity of the wind towards the coast through the vortex stretching term, while the shape

OSD
12, 3003–3041, 2015

of the coastline with capes and headlands increases the orographic effect through the vortex stretching term, tilting-twisting and turbulent flux divergence. The sea–land drag coefficient difference mainly acts as a barrier that turns the wind alongshore. Another minor factor is the sharp coastal sea surface temperature front associated with upwelling. The cool SST tends to stabilize the air column resulting in a shallower marine boundary layer that decouples from the wind aloft, inducing a weakening of the surface coastal wind. Nevertheless, a large SST anomaly (by $-3\,^{\circ}$C in their experiment) is needed to induce a significant additional wind drop-off. Therefore, the SST effect can be considered as secondary compared to the orography effect over the California coast.

In summary Renault et al. (2015) claim there is a combination of coastal topography and the presence of headlands, which induces a stronger and larger wind drop-off, which in turn is associated with a positive Ekman pumping. In a way that differs from what is observed along central-northern Chile, where the larger drop-off (Ld) length, associated with a strong wind curl (Fig. 7b and c), takes place in the presence of abrupt orography and within the Coquimbo bay system (30.25–29.25° S), where the cross-shore wind component is more intense and favors the wind curl. While with lower terrain and the presence of headlands the Ld is very small (c.f. Fig. 10, Renault et al., 2015). The origin of these differences is not well known; they may be due to several factors or processes. For example, consider that in Chile the terrain near the coast is much higher (for the coastal range and Andes mountains) than that in the west coast of USA. Furthermore, it is important to note that north of Punta Lengua de Vaca there is a local atmospheric jet with a strong diurnal cycle and seasonal variation, as a result of coastal topography that favors baroclinicity north of PLV (Garreaud et al., 2011; Rahn et al., 2011). Also, there is a possible hydraulic flow ("expansion fan") passing northward off PLV, which makes the system even more complex. This would deserve further study based on the experimentation with the regional atmospheric model, which is beyond the scope of the present study. Here the focus is on understanding possible effect of the wind drop-off and its spatial and seasonal variability on the upwelling dynamics.

OSD
12, 3003–3041, 2015

To determine the contribution of the two proposed mechanisms to the total upwelling in the region, vertical transport due to coastal divergence and Ekman pumping were meridionally integrated (from Fig. 7c and d, respectively). The contributions of different mechanisms to upwelling (Fig. 8) have a clear annual cycle with a marked semiannual component. Maximum values occur during October, with 0.23 and 0.14 Sv for Ekman transport and Ekman pumping, respectively, while the sum of both is 0.37 Sv. In addition, coastal divergence and Ekman pumping represent 60 and 40 % of the total upwelling, respectively. This indicates that Ekman transport is the stronger upwelling mechanism. However, it should be noted that these values are the sum throughout the region, and these percentages would change if specific sectors were considered especially where Ekman pumping has a larger significance (Fig. 7).

Comparing our estimates with those obtained by Aguirre et al. (2012) from QuikSCAT wind information using a larger region (~ 27.5–40° S), it is observed that coastal divergence from our study is lower, mainly because their data do not include the wind drop-off area. The winds used in their study are stronger and so are their estimates for coastal divergence (c.f. Fig. 7, Aguirre et al., 2012). However, for Ekman pumping our results are only slightly smaller than theirs. This difference is mainly due to differences in the method employed to estimate the vertical upwelling transport. In particular they use a length scale (Ld) of 150 km from the coast for their calculation, while in this study a value of 45 km was considered. However, the largest differences in the estimates of the contributions of both mechanisms to total upwelling are in the seasonal variability and the relative contribution to Ekman pumping. The seasonal variability is composed of an annual cycle with a significant semiannual component, whereas that obtained by Aguirre et al. (2012) is rather dominated by the annual cycle. This is because they make their estimates considering a larger region that includes the central-southern Chile region, where the wind has a significant annual variability. Moreover, the present results show a higher relative contribution of Ekman pumping to total upwelling in our region. This is partly due to a different technique for estimating this mechanism, the use of different wind products and the differences in the length of both study areas.

OSD
12, 3003–3041, 2015

3.4 Annual variability of Ekman pumping and its relationship with sea surface temperature near the coast

A link between SST and wind is found throughout the world ocean wherever there are strong SST fronts (see review by Xie, 2004; Chelton et al., 2007; Small et al., 2008). The link raises the questions of to what extent the wind-drop off could be associated to marked upwelling fronts in EBUS. In the context of our study, it consists in evaluating the relationship between Ekman pumping and SST, considering that the difficulty to tackle this issue is related to the fact that there is a large temporal coherence between Ekman pumping and transport, preventing a clear identification of Ekman pumping-induced SST anomalies where both processes have comparable contribution. As an attempt to identify regions where Ekman pumping has an imprint on SST, we use the Multi-Scale Ultra-High Resolution SST data set (MUR, http://mur.jpl.nasa.gov) with a spatial resolution of 1 km. Figure 9 shows the annual cycle of the MUR SST. The satellite data were compared to in situ observations that were obtained from 13 thermistors positioned close to surface along the coastline between 28–32° S (these observations were obtained by Centro de Estudios Avanzados en Zonas Aridas, Coquimbo, Chile) covering the period September 2009–September 2012. The correlations obtained between observations and satellite data were high (0.74–0.94 most values were 0.8) and the RMS between their differences was low varying between 0.54 and 1.3 °C. This provided confidence to use MUR temperatures close to the coast in the spatio-temporal analysis done in the study region. The SST results showed that south of 28.5° S there is a persistent surface cooling through all the year that increases in length (offshore) from ∼ 10 km in the northern region to ∼ 100 km in the southern region. Within this region there are prominent upwelling centers, Punta Lengua de Vaca (∼ 30.5° S), Punta Choros (∼ 29° S) and the region between 30.5–33° S. During most of the year a cold surface tongue projects offshore towards the great system of embayments of Coquimbo (SBC, with limits between ∼ 29.25 and 30.25° S), north of Punta

OSD
12, 3003–3041, 2015

Lengua de Vaca. A less intense but with a similar structure is observed north of Punta Loma de Hueso.

An illustration of the effect of Ekman pumping on SST is presented in Fig. 10 which shows the October mean spatial distribution for wind stress, Ekman pumping, SST and SST gradient. This month was selected because the maximum values of wind stress and increased surface cooling are recorded during this period. During this month, the wind stress (Fig. 10a) was intense with maximum values of $\sim 0.15\,\mathrm{N\,m^{-2}}$, showing a clear zonal gradient (drop-off) over the entire coastal band in the study area. Note that the maximum wind stress is north of the two most prominent headlands of the region (PLV and LDH), right where the wind changes direction abruptly, creating an intense cyclonic wind curl north of both ends. As the result from the distribution pattern of the wind stress, wind curl was negative in much of the area of interest resulting in a positive Ekman pumping with vertical velocities of up to $4\,\mathrm{m\ day^{-1}}$ near the coast (Fig. 10b). Also, there are two areas with a slightly negative pumping (light blue regions), following the pattern of the wind stress where the wind decreases away from the coast (see the wind vectors), producing a positive curl and a negative Ekman pumping. Moreover, as mentioned above (see Fig. 7), much of the southern spatial structure in Ekman pumping appears to be associated to the coastal terrain and abrupt changes of the coastline. A good example of this is the tongue-shaped structure that extends from the upwelled waters north of Punta Lengua de Vaca entering the Coquimbo bay system, where the upwelling induced by the Ekman transport seems not affected (Fig. 7). As the result of a positive Ekman pumping, cold water rises to surface causing a decrease in sea surface temperatures in large part of the coastal region (Fig. 10c). However, this cooling is not necessarily caused by Ekman pumping throughout the region, there are other processes that would contribute to the surface cooling that will be discussed later. Despite this, the cooling inside the Coquimbo bay system seems to be caused largely by Ekman pumping. Moreover, outside the Coquimbo bay system high values ($> 2\,^{\circ}\mathrm{C\ km^{-1}}$) of the horizontal SST gradients are distributed in a band near the coast, but not attached to it (Fig. 10d) as expected for upwelling fronts. Within the Coquimbo

OSD
12, 3003–3041, 2015

bay system, there is a homogeneous temperature zone, delimited by a less intense gradient in the west and a greater gradient in the smaller bays of the system, which coincides with the structure of an Ekman pumping tongue projected to the north of Punta Lengua de Vaca.

In order to further document the coupled spatio-temporal patterns of Ekman pumping and the SST field, a Singular Value Decomposition analysis (SVD, Venegas et al., 1997) was performed. The SVD method allows to determine statistical modes (time/space) that maximize the covariance between two data sets. Filtered time series (low pass filter with mean half-power of 280 days) and standardized of Ekman pumping and SST-MUR for the 2007–2012 period were analyzed with this method (Fig. 11). In this case the SVD analysis was successful in capturing a dominant seasonal mode. The first dominant mode accounts for 99 % of the covariance, with a 43 and 87 % of the variance explained by Ekman pumping and SST respectively. Ekman pumping spatial pattern presents maximum values very close to the coast, primarily north of Punta Lengua de Vaca, inside the Coquimbo bay system (29.3–30.2° S) and north of Punta Choros (28–29° S). Also, the pattern is intense near the coast between 30.2° S (south of PLV) and 32.5° S. The spatial pattern for SST presented areas with high variability associated with areas of maximum Ekman pumping, highlighting the overall variability in the bay system of Coquimbo and the area north of Loma de Hueso (~ 28.8° S). Moreover, the correlation between the time series of expansion coefficient was −0.96 (with R^2 = 0.92 and significant at 95 %), indicating a strong inverse relationship, consistent with that expected for a positive pumping with vertical velocities to the surface that causes a surface cooling in the region. This results in a greater contribution to the north of headlands in the region (Punta Lengua de Vaca and Loma de Hueso), even within the bay system of Coquimbo, which is consistent with the results observed in Fig. 7. Aside from the areas listed above (south of 30.2° S) the spatial pattern of SST (with greater length offshore) can not be attributed only to Ekman pumping; a significant role must be played by other processes such as the direct effect of wind, coastal divergence (Fig. 7) and vertical mixing (Renault et al., 2012), or processes related to

OSD
12, 3003–3041, 2015

mesoscale activity (filaments, meanders, eddies, etc.), which are more intense south of Punta Lengua de Vaca (Hormazabal et al., 2004), and/or ocean–atmosphere interaction (Chelton et al., 2007; Renault et al., 2015).

Summarizing, our analysis calls for more thorough study on the temperature response to wind forcing, which should involve oceanic modeling at a resolution high enough to resolve finer scale processes. The oceanic model could be forced by the high-resolution atmospheric simulations presented in this study, improving in terms of resolution previous comparable modeling for the region (Renault et al., 2012). The use of a high-resolution coupled model could be also a step further for improving our understanding of ocean–atmosphere interactions in this region. This is planned for future work.

Acknowledgements. This work was financed by Postdoctoral FONDECYT/Chile N° 3130671 and support from Centro de Estudios Avanzados en Zonas Aridas (CEAZA), Coquimbo, Chile. M. Ramos, L. Bravo and B. Dewitte acknowledge support from FONDECYT (project 1140845) and Chilean Millennium Initiative (NC120030). B. Dewitte and M. Ramos acknowledge support from FONDECYT (project 1151185). CNES (Centre National d'Etudes Spatiales, France) is thanked for financial supports through the OSTST project EBUS-South. Katerina Goubanova was supported by IRD.

References

Aguirre, C., Pizarro, O., Strub, P. T., Garreaud, R., and Barth, J. A.: Seasonal dynamics of the near-surface alongshore flow off central Chile, J. Geophys. Res., 117, C01006, doi:10.1029/2011JC007379, 2012.

Bakun, A.: Coastal upwelling indices, west coast of North America, 1946–1971, USDep. Commer., NOAA Tech. Rep., NMFS SSRF-671, Seatle, WA, 103 p., 1973.

Bakun, A. and Nelson, C.: The seasonal cycle of wind stress curl in subtropical Eastern boundary current regions, J. Phys. Oceanogr., 21, 1815–1834, 1991.

OSD
12, 3003–3041, 2015

Bane, J. M., Levine, M. D., Samelson, R. M., Haines, S. M., Meaux, M. F., Perlin, N., Kosro, P. M., and Boyd, T.: Atmospheric forcing of the Oregon coastal ocean during the 2001 upwelling Season, J. Geophys. Res., 110, C10S02, doi:10.1029/2004JC002653, 2005.
Beljaars, A. C. M.: The parameterization of surface fluxes in large-scale models under free convection, Q. J. Roy. Meteor. Soc., 121, 255–270, 1994.
Bretherton, C. S. and Park, S.: A new moist turbulence parameterization in the community atmosphere model, J. Climate, 22, 3422–3448, 2009.
Capet, X. J., Marchesiello, P., and McWilliams, J. C.: Upwelling response to coastal wind profiles, Geophys. Res. Lett., 31, L13311, doi:10.1029/2004GL020123, 2004.
Chelton, D. B., Schlax, M. G., and Samelson, R. M.: Summertime coupling between sea surface temperature and wind stress in the California Current System, J. Phys. Oceanogr., 37, 495–517, 2007.
Dyer, A. J. and Hicks, B. B.: Flux–gradient relationships in the constant flux layer, Q. J. Roy. Meteor. Soc., 96, 715–721, 1970.
Edwards, K. A., Rogerson, A. M., Winant, C. D., and Rogers, D. P.: Adjustment of the marine atmospheric boundary layer to a coastal cape, J. Atmos. Sci., 58, 1511–1528, 2001.
Enriquez, A. G. and Friehe, C. A.: Effects of wind stress and wind stress curl variability on coastal upwelling, J. Phys. Oceanogr., 25, 1651–1671, 1996.
Estrade, P., Marchesiello, P., Colin de Verdiere, A., and Roy, C.: Cross-shelf structure of coastal upwelling: a two-dimensional expansion of Ekman's theory and a mechanism for inner shelf upwelling shut down, J. Mar. Res., 66, 589–616, doi:10.1357/002224008787536790, 2008.
Garreaud, R. and Muñoz, R.: The low-level jet off the subtropical west coast of South America: structure and variability, Mon. Weather Rev., 133, 2246–2261, doi:10.1175/MWR2972.1, 2005.
Garreaud, R. D., Rutllant, J. A., Muñoz, R. C., Rahn, D. A., Ramos, M., and Figueroa, D.: VOCALS-CUpEx: the Chilean Upwelling Experiment, Atmos. Chem. Phys., 11, 2015–2029, doi:10.5194/acp-11-2015-2011, 2011.
Gill, A. E.: Atmosphere–ocean dynamics, International Geophysics Series, Academic Press, New York, 30, 403, 1982.
Halpern, D.: Measurements of near-surface wind stress over an upwelling region near the Oregon coast, J. Phys. Oceanogr., 6, 108–112, 1976.
Halpern, D.: Offshore Ekman transport and Ekman pumping off Peru during the 1997–1998 El Niño, Geophys. Res. Lett., 29, 1075, doi:10.1029/2001GL014097, 2002.

OSD
12, 3003–3041, 2015

Hong, S. Y. and Lim, J. O.: The WRF single–moment 6–class microphysics scheme (WSM6), J. Korean Meteor. Soc., 42, 129–151, 2006.
Hormazabal, S., Shaffer, G., and Leth, O.: Coastal transition zone off Chile, J. Geophys. Res., 109, C01021, doi:10.1029/2003JC001956, 2004.
Horvath, K., Koracin, D., Vellore, R., Jiang, J., and Belu, R.: Sub-kilometer dynamical downscaling of near-surface winds in complex terrain using WRF and MM5 mesoscale models, J. Geophys. Res., 117, D11111, doi:10.1029/2012JD017432, 2012.
Iacono, M. J., Delamere, J. S., Mlawer, E. J., Shephard, M. W., Clough, S. A., and Collins, W. D.: Radiative forcing by long–lived greenhouse gases: calculations with the AER radiative transfer models, J. Geophys. Res., 113, D13103, doi:10.1029/2008JD009944, 2008.
Jacox, M. G. and Edwards, C. A.: Upwelling source depth in the presence of nearshore wind stress curl, J. Geophys. Res., 117, C05008, doi:10.1029/2011JC007856, 2002.
Janjic, Z. I.: Comments on "Development and evaluation of a convection scheme for use in climate models.", J. Atmos. Sci., 57, 3686, 2000.
Jin, X., Dong, C., Kurian, J., McWilliams, J. C., Chelton, D. B., and Li. Z.: SST-Wind interaction in coastal upwelling: oceanic simulation with empirical coupling, J. Phys. Oceanogr., 39, 2957–2970, 2009.
Kalnay, E. and Coauthors: The NCEP/NCAR 40-year re-analysis project, B. Am. Meteorol. Soc., 77, 437–471, 1996.
Marchesiello, P. and Estrade, P.: Upwelling limitation by geostrophic onshore flow, J. Mar. Res., 68, 37–62, doi:10.1357/002224010793079004, 2010.
Marchesiello, P., Lefevre, L., Vega, A., Couvelard, X., and Menkes, C.: Coastal upwelling, circulation and heat balance around New Caledonia's barrier reef, Mar. Pollut. Bull., 61, 432–448, 2010.
Mellor, G. L.: Numerical simulation and analysis of the mean coastal circulation off California, Cont. Shelf Res., 6, 689–713, 1986.
Muñoz, R. and Garreaud, R.: Dynamics of the low-level jet off the subtropical west coast of South America, Mon. Weather Rev., 133, 3661–3677, doi:10.1175/MWR3074.1, 2005.
Nelson, C. S.: Wind stress and wind-stress curl over the California Current, NOAA Tech. Rep., NMFS SSRF-714, US Dept. of Commerce, Washington, D.C., 87 pp., 1977.
Paulson, C. A.: The mathematical representation of wind speed and temperature profiles in the unstable atmospheric surface layer, J. Appl. Meteorol., 9, 857–861, 1970.

OSD
12, 3003–3041, 2015

Perlin, N., Skyllingstad, E., Samelson, R., and Barbour, P.: Numerical simulation of air–sea coupling during coastal upwelling, J. Phys. Oceanogr., 37, 2081–2093, doi:10.1175/JPO3104.1, 2007.
Perlin, N., Skyllingstad, E. D., and Samelson, R. M.: Coastal atmospheric circulation around an idealized cape during wind-driven upwelling studied from a coupled ocean–atmosphere model, Mon. Weather Rev., 139, 809–829, 2011.
Pickett, M. and Paduan, J. D.: Ekman transport and pumping in the California Current based on the US Navy's high-resolution atmospheric model (COAMPS), J. Geophys. Res., 108, C103327, doi:10.1029/2003JC001902, 2003.
Rahn, D. and Garreaud, R.: A synoptic climatology of the near-surface wind along the west coast of South America, Int. J. Climatol., 34, 780–792, doi:10.1002/joc.3724, 2013.
Rahn, D. A., Garreaud, R., and Rutllant, J.: The low-level atmospheric circulation near Tongoy Bay/point Lengua de Vaca (Chilean coast 30° S), Mon. Weather Rev., 139, 3628–3647, doi:10.1175/MWR-D-11-00059.1, 2011.
Renault, L., Dewitte, B., Falvey, M., Garreaud, R., Echevin, V., and Bonjean, F.: Impact of atmospheric coastal jet off central Chile on sea surface temperature from satellite observations (2000–2007), J. Geophys. Res., 114, C08006, doi:10.1029/2008JC005083, 2009.
Renault, L., Dewitte, B., Marchesiello, P., Illig, S., Echevin, V., Cambon, G., Ramos, M., Astudillo, O., Minnis, P., and Ayers, J. K.: Upwelling response to atmospheric coastal jets off central Chile: a modeling study of the October 2000 event, J. Geophys. Res., 117, C02030, doi:10.1029/2011JC007446, 2012.
Renault, L., Hall, H., and McWilliams. J. C.: Orographic shaping of US West Coast wind profiles during the upwelling season, Clim. Dynam., doi:10.1007/s00382-015-2583-4, 2015.
Rutllant, J. and Montecino, V.: Multiscale upwelling forcing cycles and biological response off north-central Chile, Rev. Chil. Hist. Nat., 75, 217–231, 2002.
Shaffer, G., Hormazabal, S., Pizarro, O., Djurfeldt, L., and Salinas, S.: Seasonal and interannual variability of currents and temperature over the slope off central Chile, J. Geophys. Res., 104, 29951–29961, doi:10.1029/1999JC900253, 1999.
Skamarock, W. C. and Klemp, J. B.: A time-split nonhydrostatic atmospheric model for weather research and forecasting applications, J. Comput. Phys., 227, 3465–3485, doi:10.1016/j.jcp.2007.01.037, 2008.
Smith, R. L.: Upwelling, Oceanogr. Mar. Biol., 6, 11–46, 1968.

OSD
12, 3003–3041, 2015

Stark, J. D., Donlon, C. J., Martin, M. J., and McCulloch, M. E.: OSTIA: an operational, high resolution, real time, global sea surface temperature analysis system, Oceans-IEEE, 7, 1–4, 2007.

Strub, P. T., Montecino, V., Rutllant, J., and Salinas, S.: Coastal ocean circulation off western south America, in: The Sea, the Global Coastal Ocean: regional Studies and Syntheses, edited by: Robinson, A. R. and Brink, K. H., John Wiley, New York, 273–314, 1998.

Strub, P. T., Combes, V., Shillington, F., and Pizarro, O.: Currents and processes along the Eastern boundaries. in: Ocean Circulation and Climate: a 21st Century Perspective, edited by: Siedler, G., Griffies, S. M., Gould, J., and Church, J. A., Academic Press, Amsterdam, International Geophysics Volume 103, 339–384, 2013.

Sverdrup, H. U.: Wind-driven currents in a baroclinic ocean, with application to the equatorial currents of the eastern Pacific, P. Natl. Acad. Sci. USA, 33, 318–326, 1947.

Tewari, M., Chen, F., Wang, W., Dudhia, J., LeMone, M. A., Mitchell, K., Gayno, M. Ek, G., Wegiel, J., and Cuenca, R. H.: Implementation and verification of the unified NOAH land surface model in the WRF model. 20th conference on weather analysis and forecasting/16th conference on numerical weather prediction, Seattle, WA, USA, 11–15, 2004

Vazquez-Cuervo, J., Dewitte, B., Chin, T. M., Amstrong, E., Purca, S., and Alburqueque, E.: An analysis of SST gradient off the Peruvian coast; the impact of going to higher resolution, Remote Sens. Environ., 131, 76–84, 2013.

Venegas, S.A, Mysak, L. A., and Straub, D. N.: Atmos. ocean coupled variability in the South Atlantic, J. Climate, 10, 2904–2920, 1997.

Webb, E. K.: Profile relationships: the log-linear range, and extension to strong stability, Q. J. Roy. Meteor. Soc., 96, 67–90, 1970.

Winant, C. D., Dorman, C. E., Friehe, C. A., and Beardsley, R. C.: The marine layer off Northern California: an example of supercritical channel flow, J. Atmos. Sci., 45, 3588–3605, 1988.

Xie, S. P.: Satellite observations of cool ocean–atmosphere interaction, B. Am. Meteorol. Soc., 85, 195–208, 2004.

Zhang, D. L. and Anthes, R. A.: A high-resolution model of the planetary boundary layer sensitivity tests and comparisons with SESAME–79 data, J. Appl. Meteorol., 21, 1594–1609, 1982.

OSD
12, 3003–3041, 2015

Table 1. Information of the physics options and main features used in the simulations.

Parameterization	References
Microphysics: WRF Single-Moment 6-class scheme. A scheme with ice, snow and graupel processes suitable for high-resolution simulations.	Hong et al. (2006)
Longwave/Shortwave radiation: rapid Radiative Transfer Model (RRTMG). An accurate scheme using look-up tables for efficiency, accounts for multiple bands, trace gases, and microphysics species. It includes the Monte Carlo Independent Column Approximation MCICA method of random cloud overlap.	Iacono et al. (2008)
Boundary layer: University of Washington Turbulent kinetic energy (TKE) Boundary Layer scheme. This scheme is TKE based, and it is characterized by the use of moist-conserved variables, an explicit entrainment closure, downgradient diffusion of momentum, and con-served scalars within turbulent layers.	Bretherton and Park (2009)
Surface layer: based on Monin–Obukhov with Carslon–Boland viscous sub-layer and standard similarity functions from look-up tables.	Paulson (1970), Dyer et al. (1970), Webb (1970), Beljaars (1994), Zhang and Anthes (1982)
Land surface model: the NOAH Land Surface Model. For land surface processes including vegetation, soil, snowpack and land atmosphere energy, momentum and moisture exchange.	Tewari et al. (2004)
Cumulus: Betts–Miller–Janjic scheme. Operational Eta scheme. Column moist adjustment scheme relaxing towards a well-mixed profile.	Janjic (2000)

OSD
12, 3003–3041, 2015

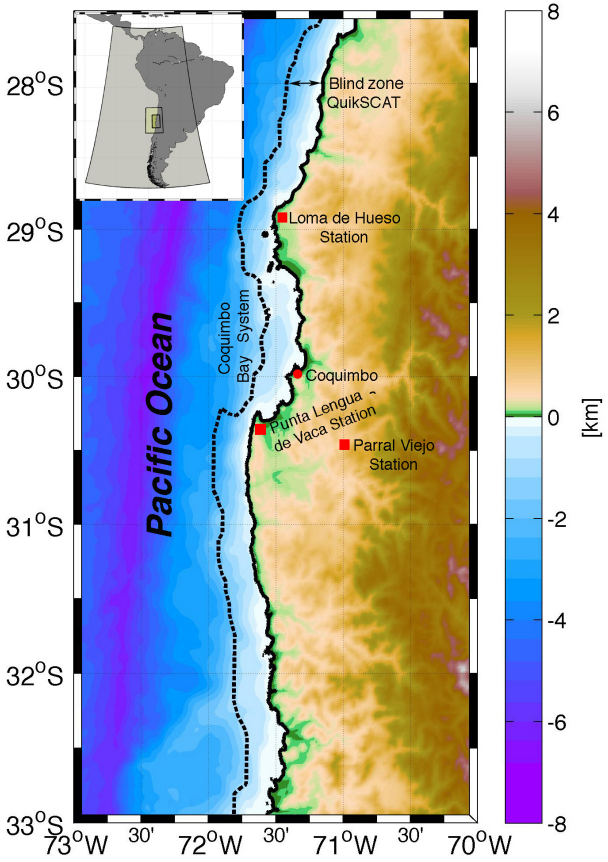

Figure 1. Study area showing bathymetry and topography of the coastal terrain. The dotted thick line indicates the western boundary of the coastal band where satellite information (~ 25 km offshore) is absent. Red squares indicate the location of the three weather stations at Loma Hueso, Punta Lengua de Vaca and Parral Viejo. The inset plot shows the three model domains used in the WRF simulations (36, 12 and 4 km).

OSD
12, 3003–3041, 2015

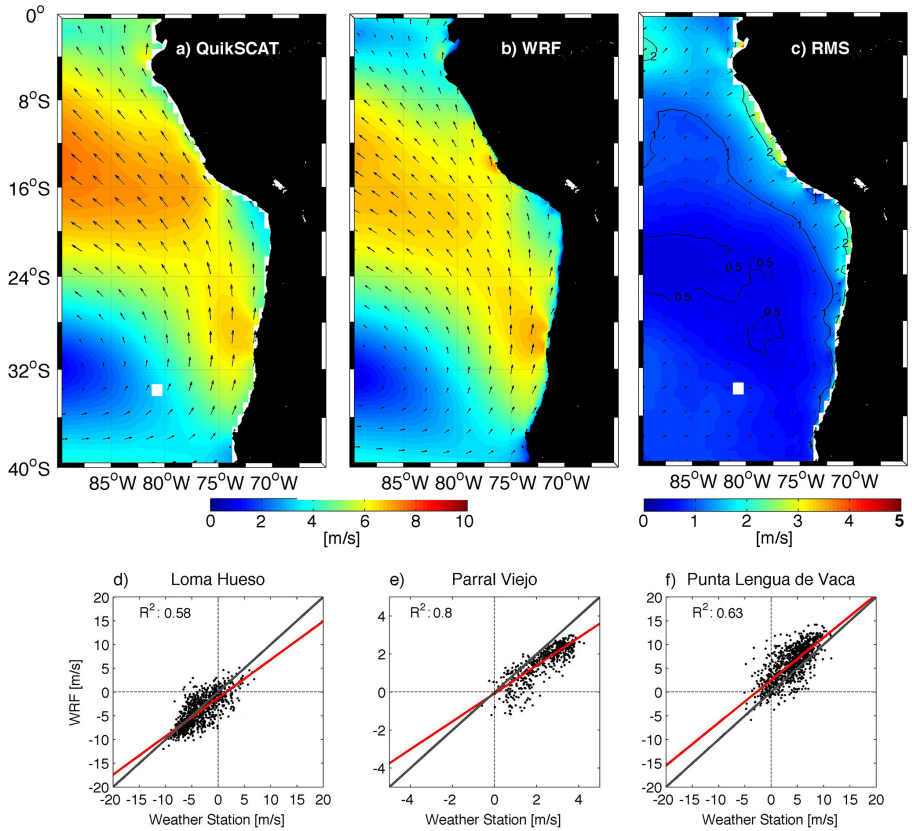

Figure 2. Comparisons of the spatial patterns of the mean velocity fields of winds obtained from **(a)** QuikSCAT **(b)** WRF simulation for the 36 km grid configuration. **(c)** Root Mean Square (RMS) differences between observations and model results. The lower panels show dispersion plots between the observed and modeled N–S winds at **(d)** Loma Hueso, **(e)** Parral Viejo and **(f)** Punta Lengua de Vaca (Fig. 1). Red line represent to linear regress and black line is 1 : 1 relation.

OSD
12, 3003–3041, 2015

Seasonal variability of the Ekman transport

L. Bravo et al.

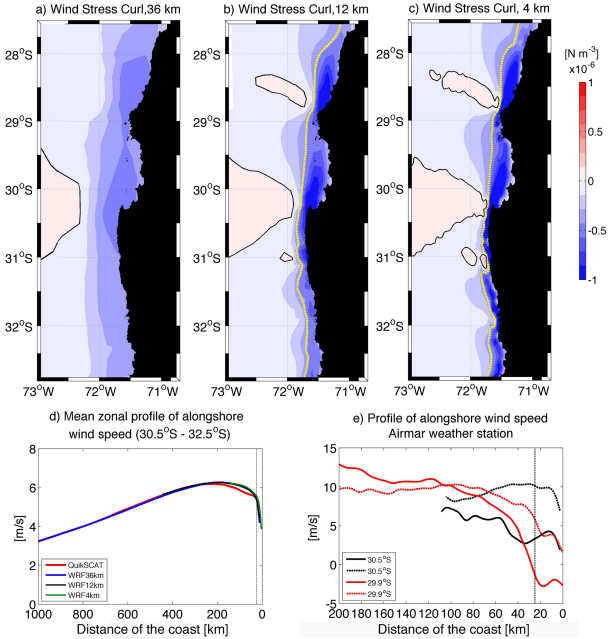

Figure 3. Mean wind stress curl obtained by the model using three model domains **(a)** 36 km, **(b)** 12 km and **(c)** 4 km. The yellow dotted line represents the length scale of the wind drop-off determined from a threshold value of -0.3×10^{-4} s^{-1} (Renault et al., 2015). **(d)** Mean zonal profiles of alongshore wind speed obtained from the three model configurations (36, 12 and 4 km) and QuikSCAT observations are shown. **(e)** Zonal profiles of alongshore wind speed from a weather station obtained onboard of a fishing boat during 2014 are also shown. The segmented line in **(d)** and **(e)** indicates the location of the satellite blind spot.

OSD
12, 3003–3041, 2015

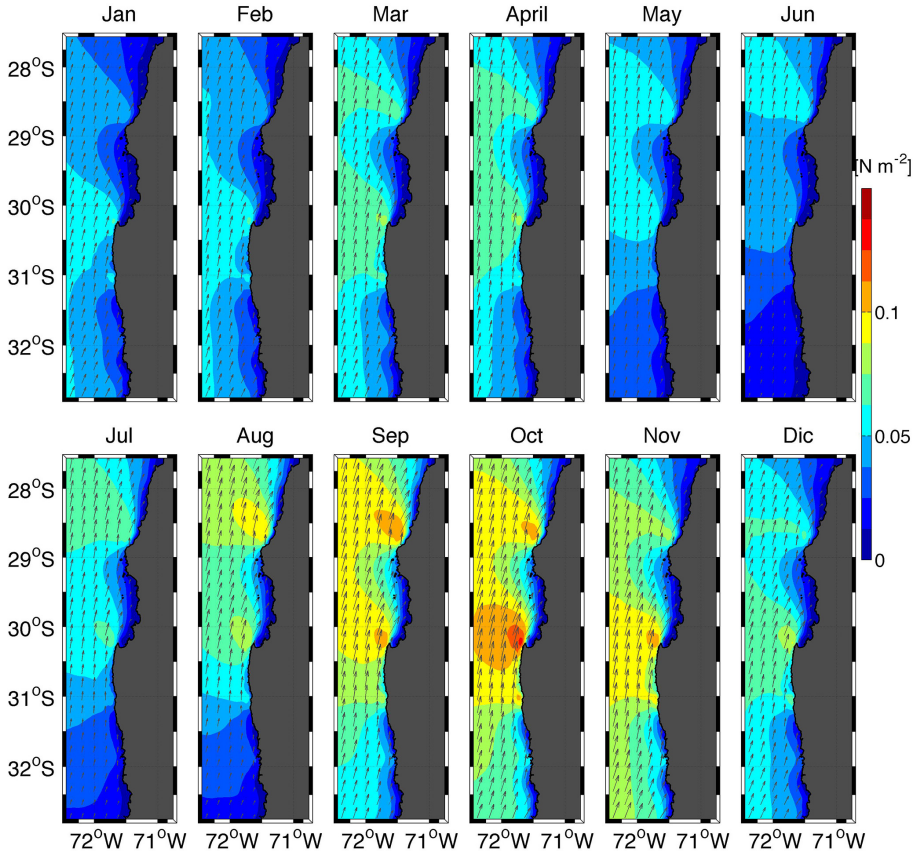

Figure 4. Wind stress annual cycle obtained from the simulation at 4 km resolution. Color represents the magnitude of wind stress (in $N\,m^{-2}$) and the arrows indicate the wind stress direction.

OSD
12, 3003–3041, 2015

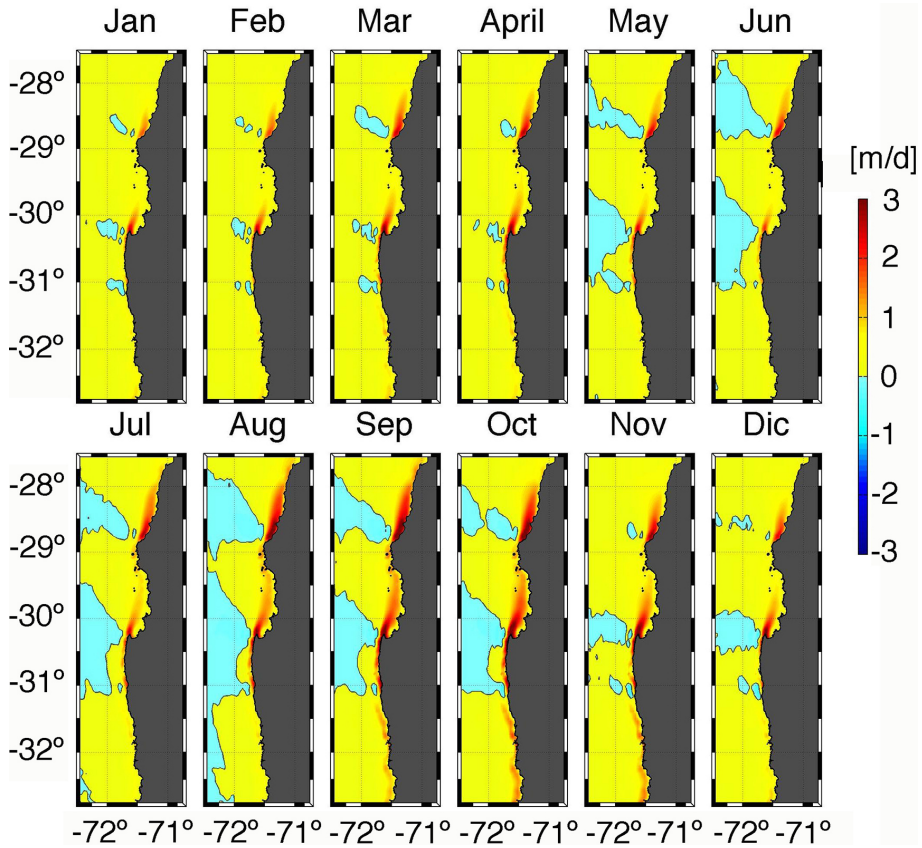

Figure 5. Annual cycle of Ekman pumping (vertical velocity in md^{-1}) obtained from the simulation at 4 km resolution.

OSD
12, 3003–3041, 2015

Seasonal variability of the Ekman transport

L. Bravo et al.

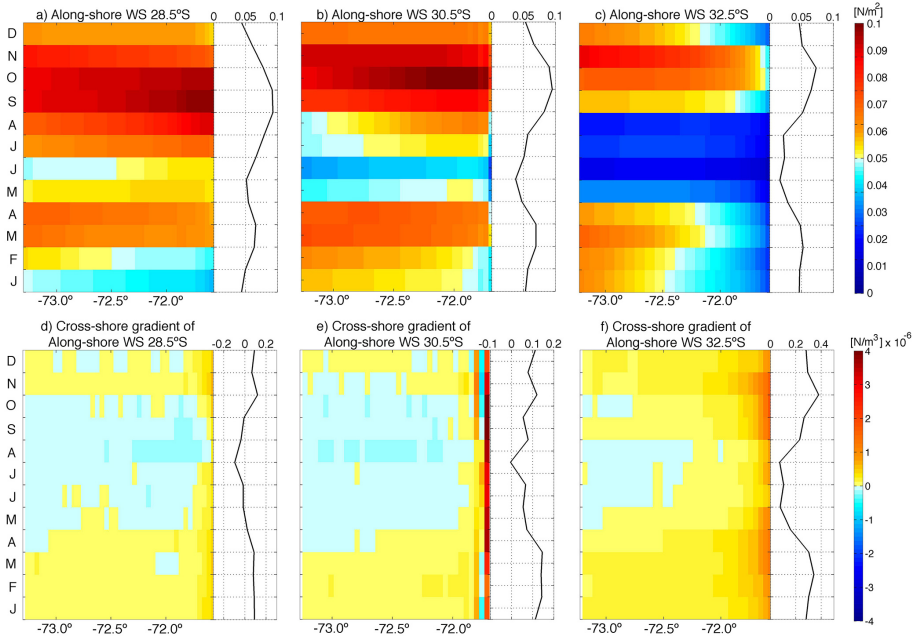

Figure 6. Hovmoller diagrams of alongshore wind stress seasonal cycle (top panels) and the zonal gradient of alongshore wind (lower panels) for the regions at 28.5° S **(a, d)**, 30.5° S **(b, e)** and 32.5° S **(c, f)**. The monthly mean zonal wind stress and mean zonal gradient are also shown (side black line).

OSD
12, 3003–3041, 2015

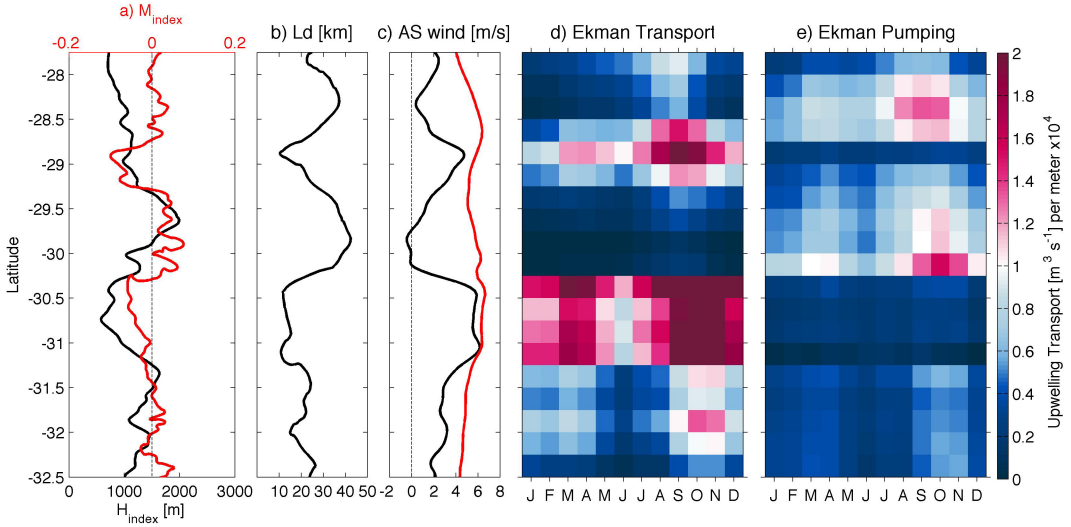

Figure 7. Contributions of the Ekman transport and Ekman pumping to the vertical transport near the coast. **(a)** Integrated orography index (H_{index}, black line) and coastaline meander index (M_{index}, red line, see text). **(b)** Drop-off spatial length. **(c)** Alongshore wind at Ld (red line) and coastal (black line). **(d)** Seasonal vertical transport associated with Ekman transport and **(e)** seasonal vertical transport associated with Ekman pumping. To estimate the Ekman transport the wind stress closest to the coast was used, while Ekman pumping was integrated from the coast to the longitude corresponding to a distance from the coast equal to the length of the drop-off (see text).

OSD
12, 3003–3041, 2015

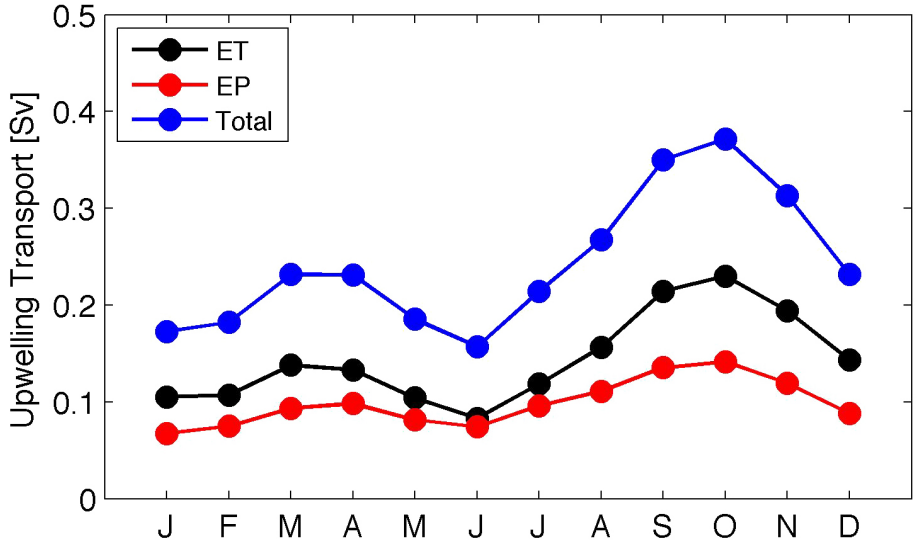

Figure 8. Contributions of Ekman transport and Ekman pumping to the vertical transport near the coast (in Sv) over the study area (27.75–32.5° S, see Fig. 7). Seasonal vertical transport associated with Ekman transport (black line), Ekman pumping (red line) and total wind induced vertical transport (blue line, sum of both vertical transports). The estimates were carried out from the WRF simulation at 4 km resolution.

OSD
12, 3003–3041, 2015

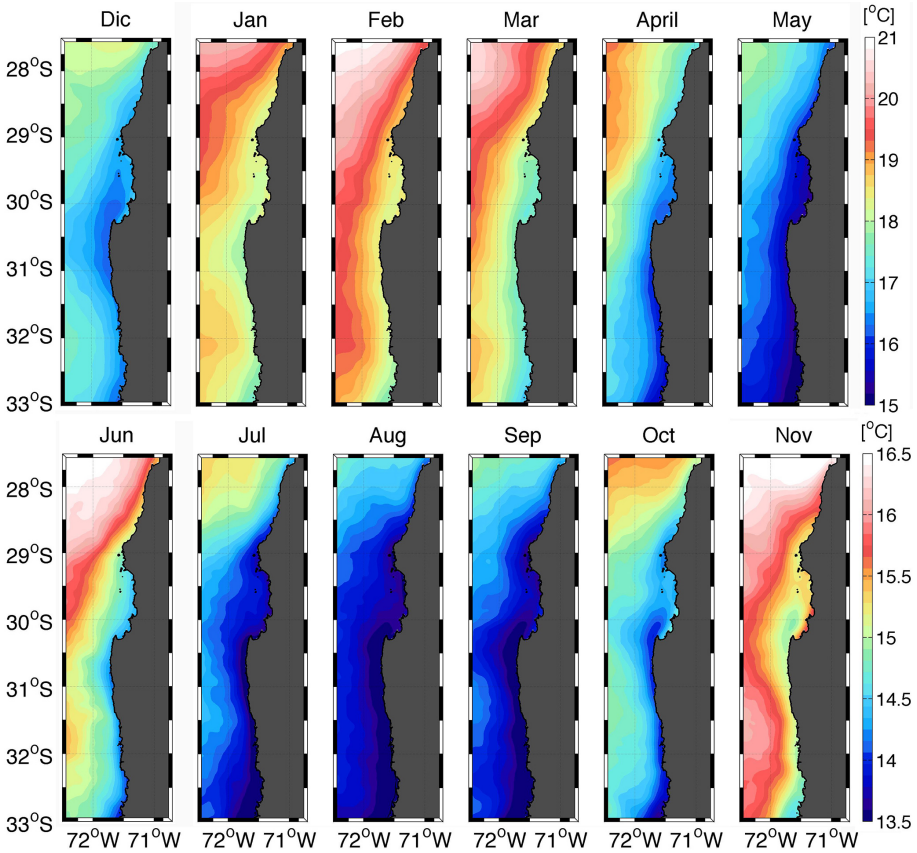

Figure 9. Annual cycle of sea surface temperature obtained using data from the Multi-scale Ultra-high Resolution (MUR). Top and bottom panels used a different colormap scale.

OSD
12, 3003–3041, 2015

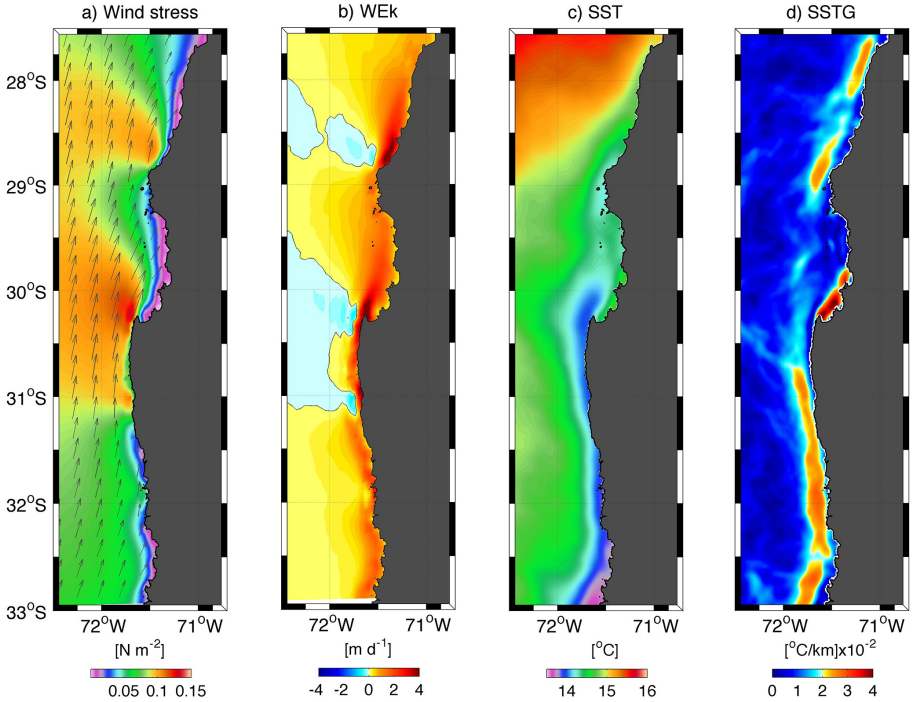

Figure 10. October mean spatial distribution for **(a)** wind stress and **(b)** Ekman pumping using the 4 km grid spacing simulation and **(c)** sea surface temperature (SST) and **(d)** SST gradient obtained from MUR observations.

OSD
12, 3003–3041, 2015

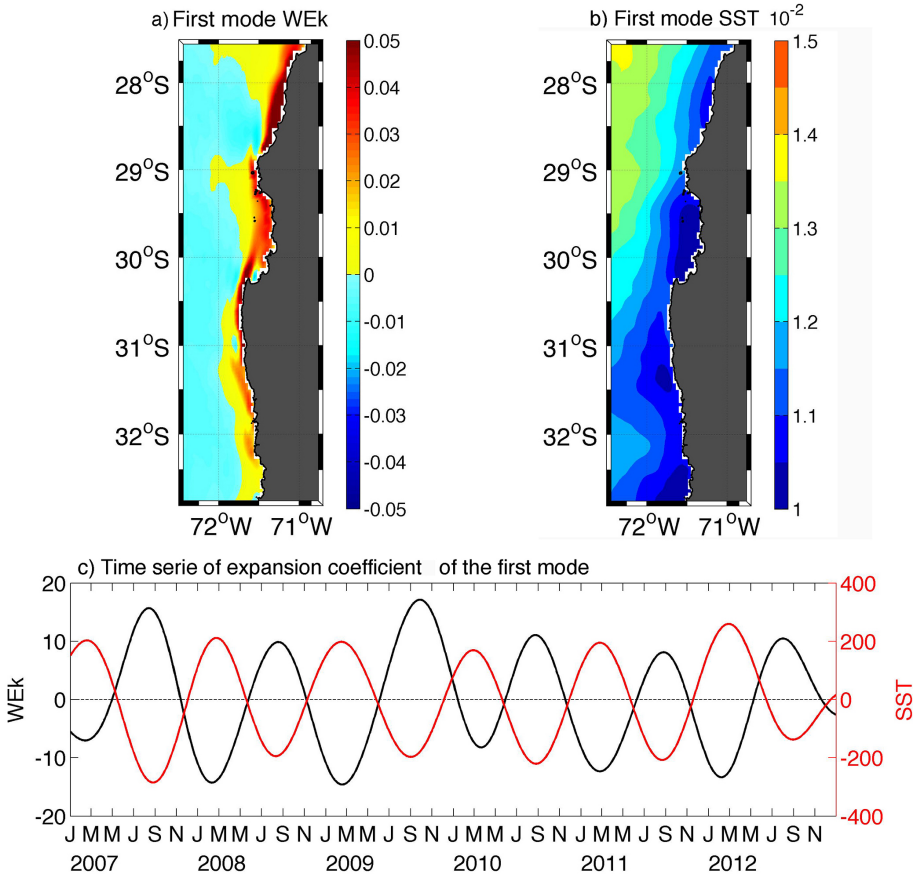

Figure 11. First SVD mode between Ekman pumping (WEk) from the WRF simulation at 4 km resolution and sea surface temperature (SST) from MUR data. **(a)** The Ekman pumping spatial component. **(b)** The SST spatial component. **(c)** The black (red) line represents the associated Ekman pumping (SST) time series. Note that the units are arbitrary.

OSD
12, 3003–3041, 2015